Composites: Part A 177 (2024) 107917

Contents lists available at ScienceDirect

Composites Part A

journal homepage: www.elsevier.com/locate/compositesa

Deconsolidation of carbon fiber-reinforced PEKK laminates: 3D real-time *in situ* observation with synchrotron X-ray microtomography

Luc Amedewovo [a], Laurent Orgéas [b], Basile de Parscau du Plessix [a], Nicolas Lefevre [a], Arthur Levy [a,*], Steven Le Corre [a]

[a] Nantes Université, IRT Jules Verne, CNRS, Laboratoire de thermique et énergie de Nantes, LTeN, UMR 6607, F-44000 Nantes, France
[b] Univ. Grenoble Alpes, CNRS, Grenoble INP, 3SR Lab, 38000 Grenoble, France

ARTICLE INFO

Keywords:
A. Porosity
B. Residual/internal stress
E. Out of autoclave processing
D. CT analysis

ABSTRACT

Deconsolidation of carbon-fiber reinforced thermoplastic laminate occurs while (pre)heating the materials during their forming processes. Pores nucleate, grow and lead to degradations of mechanical properties. Here, a new experimental device was developed and installed inside a synchrotron beamline (dedicated to fast X-ray microtomography). Pore nucleation and growth was observed in 3D, real-time and *in situ* while heating Carbon/PEKK laminate samples. The time evolution of sample deconsolidation strain, porosity, as well as number, size and morphology of pores was assessed. Nucleation and growth is observed above the glass transition temperature and enhanced with initial moisture content. Drastic deconsolidation when approaching melting temperature is thought to be driven by internal stress in the laminate. The data provided may be used as input for modeling purposes or for validation of existing models.

1. Introduction

High-performance thermoplastic composites (TPCs) are promising materials for the aerospace industry, given their many advantages, such as weldability, unlimited shelf (storage) life, good mechanical properties and chemical resistance. While manufacturing and assembling, these materials may be subjected to deconsolidation, *i.e.*, the nucleation and growth of pores during the heat-assisted forming processes of pre-consolidated TPC laminates. Deconsolidation usually occurs when laminates are subjected to sufficiently low confining pressure during the heating stage and leads to a final composite part with, at times, substantial and detrimental porosity. Several works have already shown a significant degradation of mechanical properties when the composite porosity overcomes critical volume content [1–3]. In order to avoid such a porosity, a good understanding of deconsolidation phenomenon is necessary.

The mechanisms of pore nucleation and growth in high-performance TPCs are complex and raise different hypotheses in literature. A first possible explanation of deconsolidation is related to the initial moisture and volatile contents in the laminates. This assumption was inspired by the findings made during the forming of thermoset composites: moisture was one of the main causes of deconsolidation [4–6]. Indeed, increasing the temperature up to the sample heating stages leads to an increase of water vapor pressure which exceeds the confining pressure the composite may be subjected to, and thus causes pore nucleation and growth through moisture diffusion. Considering that thermoplastic polymers also uptake moisture when exposed to a humid environment, this hypothesis was used to explain the deconsolidation observed with some glass fiber-reinforced TPCs (GF/PP, GF/PEI) [7–9]. In the case of high-performance TPCs, this hypothesis was also supported by Slange et al. [10] after carrying out deconsolidation experiments with dried and undried UniDirectional (UD) layered $[0/90]_{4s}$ Carbon Fiber/PolyEtherEtherKetone (CF/PEEK) laminates, which were pre-consolidated with a 1 MPa confining pressure. The authors showed that the thickness increase induced by the deconsolidation of the dried samples was significantly lower than that of the undried ones. Consequently, the authors recommended drying the laminates at 250°C for 3 h prior to processing.

A second possible origin of deconsolidation was inspired by the findings on porosity growth in woven and mat TPC laminates. Related works showed that internal stresses stored in the laminates during their fabrication, *e.g.*, the elastic energy of the fibrous networks stored after their pre-compaction and cooling down, could also be another important driving force for deconsolidation [11–13]. Indeed, while heating the aforementioned consolidated composites, polymer melting allows such internal stresses to be released, thus enhancing porosity growth [14]. In the case of high-performance TPCs, this hypothesis was

* Corresponding author.
E-mail address: arthur.levy@univ-nantes.fr (A. Levy).

https://doi.org/10.1016/j.compositesa.2023.107917
Received 24 July 2023; Received in revised form 16 November 2023; Accepted 17 November 2023
Available online 24 November 2023

supported by Donadei et al. [15] after carrying out deconsolidation experiments on annealed and non annealed layered UD $[-45/90/45/0]_{3S}$ CF/PolyEtherKetoneKetone (PEKK) laminates consolidated at 0.6 MPa in an autoclave: drying at 240°C for 3 h was not sufficient to prevent deconsolidation. The authors showed that annealing at 240°C for 20 h was required to relax internal stresses, in order to avoid deconsolidation.

These different conclusions suggest that both the initial moisture content and internal stresses, both stored in the consolidated laminates during their fabrication, may be involved in deconsolidation mechanisms of TPCs. Since drying and internal stress release are prone to occur altogether, it is difficult to decorrelate/understand these two effects without fine scale *in situ* observation. Indeed, the post-process techniques (thickness measurement, micrographs, *etc.*) used to characterize deconsolidation in these studies [10,15] are interesting but do not allow a proper analysis of what happens during heating and dwell [16]. Another interesting technique used to characterize porosity in composites is *ex situ* 3D imaging using X-ray microtomography [17]. In contrast with 2D micrographs, this technique allows 3D characterization of pores, including their volume content, shape and spatial distribution. However, scanning times of laboratory microtomographs are too long to provide relevant real-time and *in situ* observation of microstructure changes during composite processing [18].

The development of synchrotron X-ray tomographs has made the real-time and *in situ* observation of microstructure evolution [19–21] possible during the forming processes of composite materials without the need to interrupt the processing cycle [22]. Another interesting study is the work carried out by de Parscau et al. [23] in order to study pore nucleation and growth during the heating of fiber-reinforced thermoset composites. Their work demonstrated the ability of synchrotron X-ray microtomography to characterize in real-time (via short scanning times) important 3D structural parameters (such as pore shape, size and spatial distribution) that are difficult to measure with other experimental techniques. Thanks to those unique advantages, this technique has been used several times in the literature to study curing issues in thermoset composites [24–27]. However, to our knowledge, there is no available study of deconsolidation of high-performance thermoplastic processing using fast *in situ* X-ray tomography. This could be due to the processing conditions of high-performance TPCs which are more severe than those of thermoset composites, *i.e.*, requiring high temperatures (330°C–400°C).

Thus, within this context, we developed a new experimental device to perform deconsolidation experiments under representative conditions of high-performance TPC processing while allowing 3D real-time and *in situ* images by using fast X-ray synchrotron microtomography. We could thus observe and quantify the nucleation and growth of pores during the representative heating of high-performance TPC laminates CF/PEKK.

2. Materials and methods

2.1. CF/PEKK composite manufacturing

The laminates used in this study were produced using unidirectional CF/PEKK 7002 prepreg plies supplied by Toray Advanced Composites. The plies have a fiber areal weight of 194 g m^{-2} and a theoretical thickness of 0.185 mm. The PEKK mass content is 34%. According to the manufacturer, its glass transition temperature T_g, melting temperature T_m and crystallization temperature T_c are 160°C, 337°C, and 265°C, respectively. In practice, the melting zone for the neat polymer, observed during Differential Scanning Calorimetry experiments with a heating ramp of 5°C / min, ranges between 310°C and 360°C, with a melting peak at 338°C [28–30]. Besides, during cooling at 10°C / min, the crystallization zone extends between 240°C and 283°C, with a crystallization peak at 269°C, for the matrix alone [28–30]. Using the prepreg plies, unidirectional $[0]_{16}$ (UD) and cross ply $[0/90]_{4S}$ (CP) laminates of 350 mm × 350 mm × 2.90 mm containing 16 plies were manufactured by hot press consolidation. The consolidation was carried out in a 50 t Pinette P.E.I press by using a picture-frame mold and according to the following cycle: heating at 10°C min^{-1} up to 380°C under a confining pressure of 0.1 MPa; isothermal holding for 20 min under a confining pressure of 4 MPa; cooling at 10°C min^{-1} at the same pressure, then demolding.

2.2. Preconditioning

In order to investigate the role of moisture during deconsolidation, 20 mm diameter cylinders were cut out from the consolidated laminates using a Protomax waterjet cutting machine and separated into two groups: Dried Samples (DS) and Water Immersed samples (WI). DS samples were heated at 180°C for 72 h in order to restrain initial moisture content. A continuous weight measurement during drying experiments at different temperatures proved that this drying condition eliminated the effect of moisture without any thermal degradation of the material: no further significant weight change was observed at 180°C after this duration. For further details, the reader may refer to our previous work [31]. WI samples were immersed in distilled water at room temperature (≈ 23°C) for 3 months before the experiments. A weight measurement of the samples before and after the immersion showed that the relative moisture weight content of the immersed samples was 0.1% at the end of the immersion.

2.3. Experimental setup

To observe the microstructural changes in the laminates during the deconsolidation experiments, we developed a specific device. The setup functions are twofold: to subject samples to temperature and pressure cycles which are representative of TPC laminates processing conditions, while allowing 3D real-time *in situ* observations of the sample microstructures with synchrotron X-ray microtomography. For that purpose, the setup was designed to be mounted onto the rotation stage of the ID19 beamlime tomograph (ESRF, France). As illustrated in Fig. 1, the device was composed of two cylindrical copper hot platens which can heat up to 450°C with a maximal heating rate of 2°C s^{-1}. The temperature of the hot platens was measured by K-type thermocouples located in the middle of each hot platen, 1 mm beneath their surfaces. The platen heating was achieved with one resistive cartridge of 200 W placed in each hot platen, and regulated by two 3508 Eurotherm PID temperature controller. 30 mm thick calcium silicate thermal insulators were placed between the hot platens and the other components, in order to restrain the thermal expansion of the whole setup during the experiments. To limit convective heat losses, samples were also confined by a thin aluminum tube (0.5 mm thickness) with a low X-ray absorption. In addition, to improve the image contrast at the sample boundaries, an aluminum disk was placed between the sample and the lower hot platen. A pneumatic actuator (CDQMB25-25 from SMC) was placed on top of the upper hot platen. It can apply a confining pressure of up to 1.2 MPa on tested samples. This capability was used here only for the analysis of the reconsolidation phenomenon. A central plate was placed between the actuator and the hot platen to enhance the transmission of the piston load to the hot platen. Since the device is rotating during imaging, all power cables and thermocouple wires were connected to a SVTS C 03 slip ring connector provided by Servotecnica. The slip ring allowed the compressed air supply during the rotation too. The upper part of the device was supported by three aluminum tubes (0.5 mm thickness) connected to the lower support. Lastly, during the experiments, the pressure was regulated by a pressure controller supplied by Festo (vppm-6l-l-1-g18-0l6h-v1p-s1c1). The temperature data acquisition and control were performed automatically using a KEYSIGHT 34972 A data acquisition unit provide by Agilent and Eurotherm itools software. This allowed full control of the experiment conditions (heating rate, temperature, and pressure).

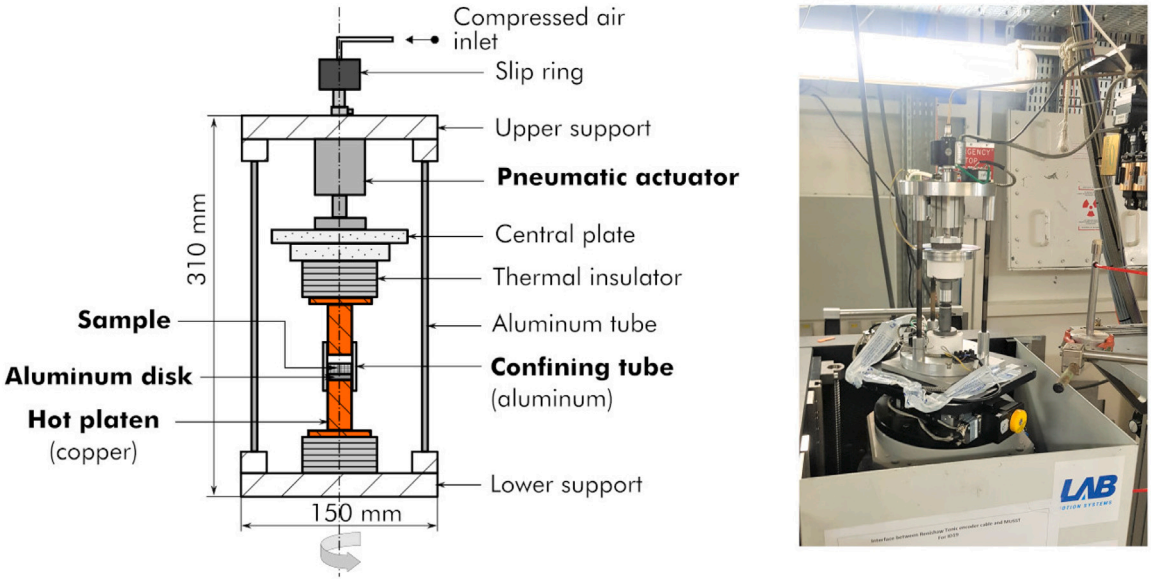

Fig. 1. *In situ* Composite Deconsolidation Tomography Observation setup. Schematic view (left) and picture of the device installed onto the rotation stage of the ID19 beamline X-ray microtomograph (right).

Table 1
Testing conditions used for deconsolidation experiments.

Test #	Laminate	Conditioning	Pressure	Dwell time	Heating type	Label
1	UD	WI	NAP	10 min	two-sided	UD-WI-2SH
2	UD	DS	NAP	10 min	two-sided	UD-DS-2SH
3	CP	WI	NAP + P_R = 0.1 MPa	10 min + 10 min	two-sided	CP-WI-2SH
4	UD	WI	NAP + P_R = 0.05 MPa	10 min + 5 min	one-sided	UD-WI-1SH

2.4. Deconsolidation experiments

The deconsolidation tests consisted of heating samples at 60°C min^{-1} up to a first dwell at 120°C for 5 min followed by a heating at 10°C min^{-1} up to a second dwell at 380°C for 10 min. The first dwell allowed for the same reference temperature for the scans start-up. To check the effect of thermal gradients on deconsolidation, samples were heated either by one hot platen only (one-sided heating, 1SH) or by both hot platens simultaneously (two-sided heating, 2SH). Also, sample were either (i) let free, *i.e.*, with No Applied Pressure (NAP) where a gap of 3 mm was kept between the sample and the upper platen, or (ii) subjected to a given constant confining pressure. More precisely, to observe pressure effects on the reduction of porosity content after free deconsolidation, a re-consolidation pressure P_R was applied during the second dwell at 380°C (NAP + P_R). In this case, the dwell time was extended from 10 min to 15 min or 20 min so that the re-consolidation pressure was maintained for 5 min or 10 min. The complete investigated testing conditions are summarized in Table 1.

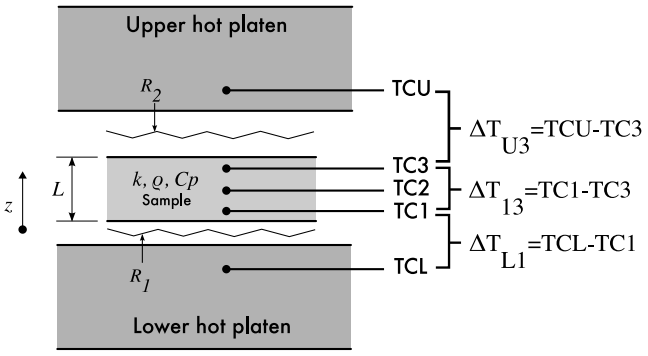

Fig. 2. Estimation of the effective laminate temperature using a through thickness 1D heat transfer model. The model is fitted using 5 thermocouple measurements. R_1 and R_2 represent the thermal resistances between (i) the lower hot platen and composite lower face and (ii) the composite upper face and the upper hot platen.

2.5. Estimation of the sample temperatures during the experiments

During the deconsolidation tests, the temperature measured by the thermocouples inserted in the hot platens are not representative of the sample temperatures. On the one hand, this is due to the gap of 2 mm left between the upper hot platen and the sample. On the other hand, the aluminum disk placed between the sample and the lower hot platen also induces thermal contact resistance. For a proper analysis of the thermomechanical conditions of deconsolidation, the temperature inside the composite sample has to be estimated more accurately. A conductive heat transfer model was thus developed and calibrated to estimate the temperature distribution in the samples. For that purpose, we used two specimens which were instrumented with three embedded K-type thermocouples and loaded using one-side and two-side heatings (Fig. 2). One thermocouple was located at the sample center (TC2) and the others two plies deep (≈ 0.4 mm) underneath the sample upper (TC3) and lower face (TC1). The temperature measurements during the heating cycle of the deconsolidation experiments (described in Section 2.4) are shown in Fig. 3.

First, a significant temperature difference ΔT can be observed between the hot platens and the center of the composite sample, during the heating for both configurations. The temperature difference ΔT_{L1} between the lower hot platen (TCL) and the sample lower face (TC1) as well as the temperature difference ΔT_{U3} between the upper hot platen

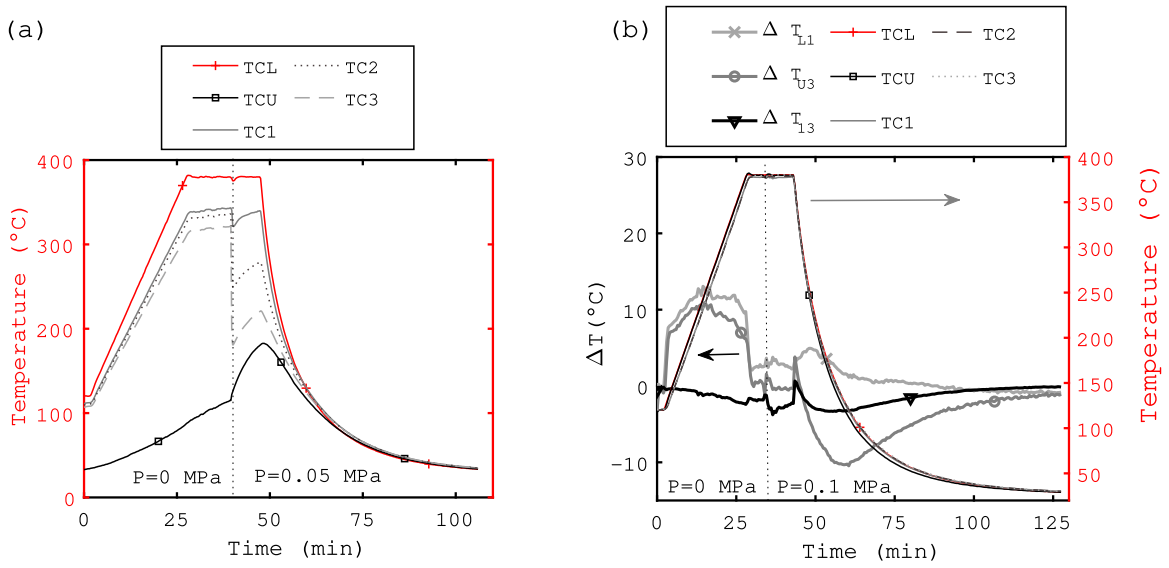

Fig. 3. Thermocouple measurements during one-sided heating with natural cooling (a) and two-sided heating with enforced cooling (b) cycle of deconsolidation experiments. On the right graph (b) the temperature is much more homogeneous. Temperature differences are plotted along the left axis. We can see the thermal effect of pressure application during dwell.

(TCU) and the sample upper face (TC3), are largely higher than 10°C during the heating stage. This temperature difference is due to the thermal contact resistances mentioned earlier and the non-isothermal heating during one-sided heating.

Secondly, the application of pressure during the dwell causes a decrease in the temperature difference between the hot platens and the sample: pressure improves the contact at the interfaces and thus promotes better heat transfer. However, in the case of one-sided heating (1SH), the application of pressure also leads to an increase in the temperature gradient in the sample (Fig. 3 a). This is due to the fact that the upper hot platen is initially cold.

Finally, the temperature difference ΔT is much smaller during cooling in the case of one-sided heating (Fig. 3 a) compared with the case of two-sided heating (Fig. 3 b). This difference is related to the fact that in the case of one-side heating, the sample was cooled by natural convection with the ambient air. In the case of two-side heating, the sample was cooled rather by forced convection, by blowing cold air (≈ 20°C) on the edges of the hot platens. Forced convection results in a greater temperature difference by causing rapid cooling of the copper hot platens.

The temperature cycles presented here correspond to the thermal cycle experienced by the samples during the deconsolidation tests at ESRF. The experimental temperature measurements were used to validate the thermal model described in Appendix A.

2.6. 3D real-time in situ imaging

During the experiments, tomographic scans were performed. For that purpose, fast scans of 1 s were carried every minute. These scans consisted of 2016 X-ray 2D projections obtained by an incremental rotation along the vertical axis of the rotation stage with a beam energy of 66 keV. The resulting 3D grey level images were reconstructed from the 2D X-ray projections using standard reconstruction algorithms combined with the Paganin method [32] to enhance the constrast between imaged phases. The reconstructed 3D grey level images represent volumes of 7.68 mm × 7.68 mm × 5.37 mm with a voxel size of 3.81^3 μm^3.

To extract quantitative (micro)structural descriptors from these images, we used the freeware Fiji [33] together with the SimpleITK and panda libraries [34] (Python). Hence, at the macroscale and from the grey level vertical slices of the 3D images (see Fig. 4), we used the "Multi-point" tool of Fiji to measure manually at 10 various locations the sample thicknesses. These data were then averaged to estimate the mean sample thickness and the natural macroscopic deconsolidation strain $\varepsilon_D = \ln(l/l_0)$, where l_0 and l correspond to the initial and current mean sample thicknesses, respectively. At the microscale, additional analyses were performed with Regions Of Interest (ROIs) of horizontal surface 3.81 mm × 3.81 mm picked from the 3D images. Since the thickness of the samples varied with increasing temperature, the thicknesses of the ROIs were also variable (Eulerian tracking). The ROI thicknesses were thus obtained by cropping the sample cores. The limits of the cropping frame were located one ply deep (≈ 0.2 mm) underneath the sample upper and lower boundary (Fig. 4 a, b). The as-cropped ROIs were then segmented using the trainable Weka segmentation algorithm [35] implemented in Fiji (Fig. 5) in order to extract the pores from the solid phases (polymer+carbon fibers). Finally, the pores having a size of one voxel were discarded as they may be noise or artifacts.

Therewith, the porosity ϕ (resp. ϕ_z) of the ROIs (resp. along the thickness of the ROIs) could be estimated as the ratios of the number of the pore voxels in the ROIs (resp. in the stack located at a given height z) over the number of the voxels of the ROIs (resp. of the considered stack). In addition, based on the Euclidean distance map of the SimpleITK library, we could also label the pores and thus estimate their number. Dividing the number of pores by the ROI volume enabled us to estimate the number of pores $\mathcal{N}_p$ per unit of volume (named pore density hereafter).

By using the same library, each labeled pore was also fitted with an Oriented Bounding Box (OBB) of dimensions a (length), b (width), and c (height) ($a > b > c$) from which two geometrical aspect ratios were estimated, namely the OBBs elongation el (b/a) and flatness fl (c/b) [36]. The pore morphologies were then classified in four classes: sphere-like if $el > 0.7$ and $fl > 0.7$; blade-like (or ellipsoidal) if $el < 0.7$ and $fl < 0.7$; disk-like (or oblate) if $el > 0.7$ and $fl < 0.7$; and rod-like (or prolate) if $el < 0.7$ and $fl > 0.7$ [37]

3. Results

3.1. Qualitative analysis

The vertical grey level slices displayed in Fig. 6 show the time evolution of the dried UD sample (DS) structure during two-sided

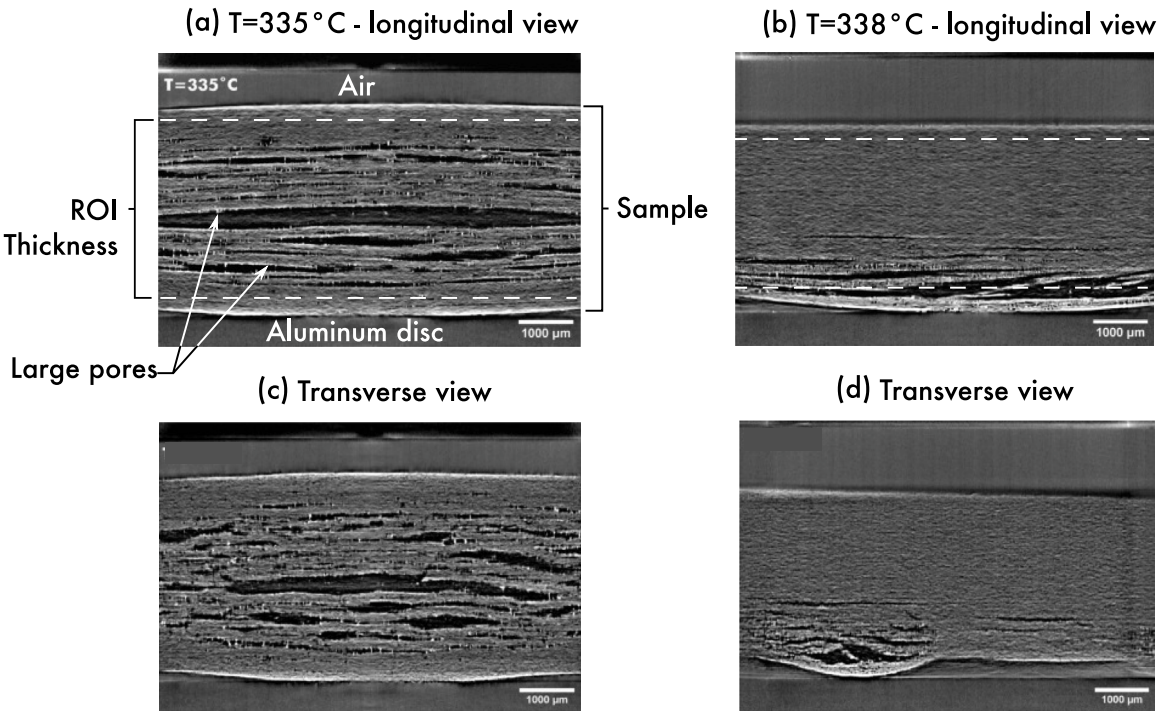

Fig. 4. 2D grey level slices through the thickness of a deconsolidated UD laminate showing the ROI thickness and pore during two-sided heating (a,c) and one-sided heating (b,d). The slices are parallel to the fibers' orientation in (a,b) and transverse to the fibers in (c,d).

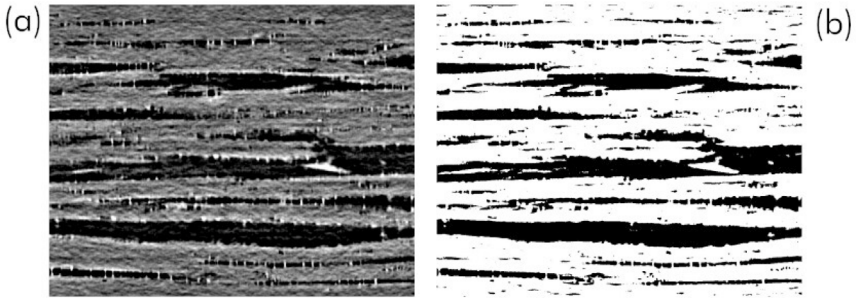

Fig. 5. Comparison between a grey scale (a) and segmented (b) slice parallel to the fibers' orientation, through the thickness of a deconsolidated laminate. The black zones represent the pores.

heating (2SH) and cooling. A first phase is observed up to 323°C, with a small increase in the sample thickness without marked occurrence of pores. This is presumably related to the sample thermal expansion. A second phase of deconsolidation can be observed above 323°C. It is characterized by a marked and rapid increase in the sample thickness (Fig. 6 d). During this phase, large pores appear and lead to a visible decohesion between the plies of the laminate. Such pore growths are systematically associated with the tension and the rupture of thin PEKK filaments which are also well-observable in the slice (d) (in white), these two features also being visible in Figs. 4 and 5. It is also worth noting that the external surface exhibits non-zero valued curvature. During the dwell at 380°C, Fig. 6 e shows that the large pores subsequently tend to collapse, leading to noticeable decreases of both the sample thickness and the curvatures of its external surfaces. The gas potentially trapped in the pores is assumed to find a pathway to the perimeter and escape the specimen, especially given the relatively small sample diameter. Gravity effects may also help this collapse. Finally, upon cooling, a slight decrease in the sample thickness is also observed and probably ascribed to thermal and crystallization shrinkages (Fig. 6 f). The complete evolution of the slice related to this test as well as those of the three other tests are provided as video files in the supplementary materials.

Typical evolutions of the amount, size and distribution of pores during deconsolidation are illustrated with the 3D segmented images shown in Fig. 7 in the case of the DS sample. Firstly, it is interesting to note a small but clearly visible amount of micropores are (initially) entrapped in the composite at T = 120°C (Fig. 7 a). This porosity probably comes from the consolidation process during which it is difficult or even impossible to obtain a perfectly consolidated laminate without porosity. This porosity content was not measurable with the 2D optical micrographs reported in [16] and performed with similar spatial resolution (pixel size 1.55 μm^2): this could presumably be induced by some possible artifacts induced during the polishing used to obtain the 2D micrographs. In addition, as the temperature rises to 323°C, the amount of porosity increases, with (i) more and more small pores and (ii) the occurrence of medium-sized pores (Fig. 7 b–c). Between 323°C and 335°C, a very fast and drastic increase in porosity is recorded with, in particular, many large-sized pores which are the signature of interply decohesion (Fig. 7 d). As evidenced before, during the dwell, the large-sized porosities collapse and probably split into smaller pores (Fig. 7 e). No significant change in the microstructure is observed during cooling (Fig. 7 f). The complete porosities evolution during the other tests is also provided as video files in the supplementary materials. We have also reported a similar example in Fig. 8 on the cross-ply (CP) laminate

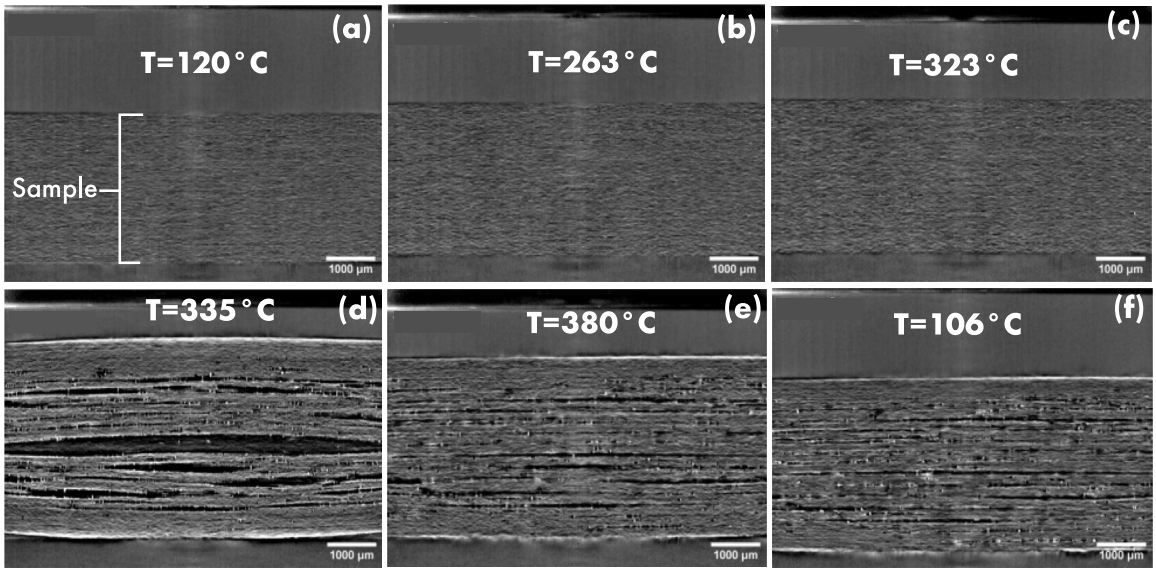

Fig. 6. Tomographic cross section evolution over a temperature cycle of an initially dried $[UD]_{16}$ composite sample for 72h@180°C (UD-DS-2SH). The black spots represent the pores.

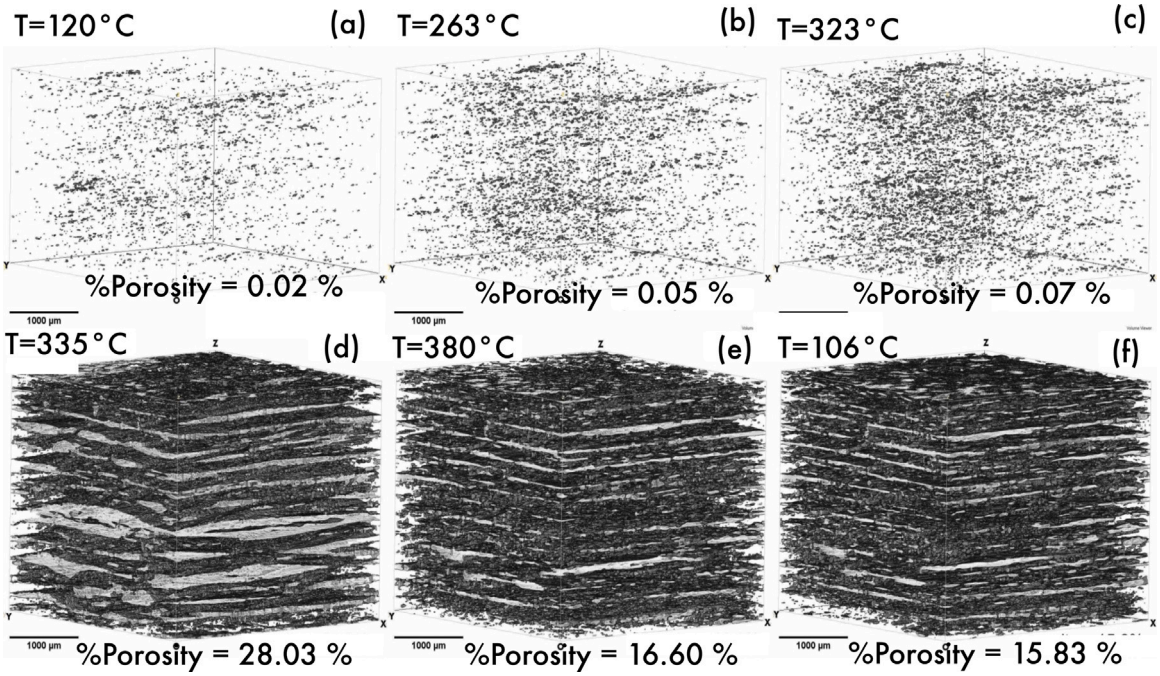

Fig. 7. Time evolution of the porosity in a ROI of 3.81 mm × 3.81 mm × Z during deconsolidation of an initially dried $[UD]_{16}$ composite sample for 72h@180°C. The axis (OX) and (OY) are respectively parallel and transverse to the fibers' main axis. The black spots represent the pores.

case, initially stored in distilled water (WI). The same phenomena can be observed at first glance. The focus is made here on the application of a 0.1 MPa pressure during the isothermal dwell (Fig. 8 d-f). A very fast reconsolidation, almost instantaneous when the pressure is applied, can be observed. The porosity is drastically reduced. However, residual porosity with small or medium-sized pores remains at the end of the cooling process (Fig. 8 f), with a progressive and slow decrease in porosity related to a consolidation process.

3.2. Quantitative analysis at the sample scale

The temperature evolutions of the sample deconsolidation strain ε_D and the porosity ϕ inside the ROIs are reported in Fig. 9, from which three stages can be distinguished:

- For all tests, stage 1 is observed at low temperatures. Herein, the deconsolidation strain ε_D slightly increases (practically linearly) and where the porosity ϕ does not significantly increase. As assumed previously, this stage could *a priori* be related to the thermal expansion of the samples. For the tests carried out in dried (DS) or wet (WI) conditions with two-sided heating (2SH), we roughly estimated from the $\varepsilon_D(T)$ curves of Fig. 9 (a–b) respective apparent out-of-plane thermal expansions (above $T_g \approx$ 160°C) of 100.3 10^{-6} K^{-1} and 179.1 10^{-6} K^{-1}, *i.e.*, two values which are in-line with that measured from standard dilatometry with a sample stored at 20%RH, *i.e.*, 139.4 10^{-6} K^{-1} [16] and suggesting that the higher the initial water content, the higher the apparent thermal expansion. The trend could be explained by a closer look at the temperature evolutions of the sample porosity

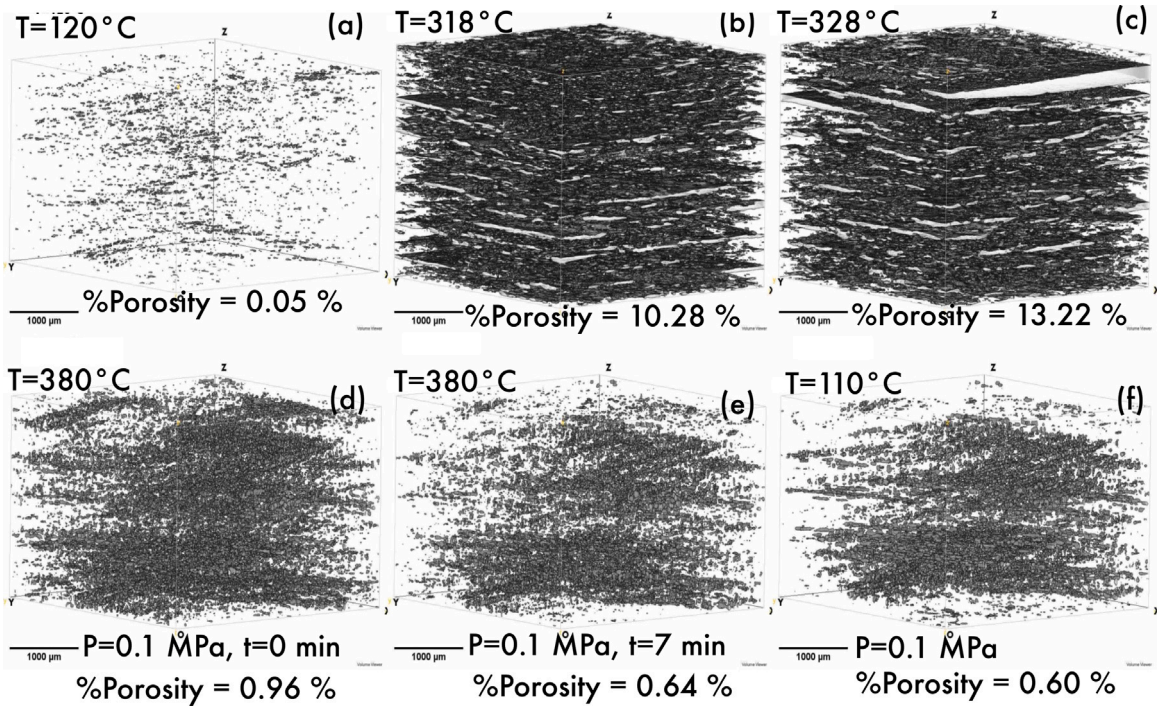

Fig. 8. Time evolution of the porosity in a ROI of 3.81 mm × 3.81 mm × Z pixels during deconsolidation of an $[0/90]_{4S}$ cross-ply laminate sample initially stored in distilled water. The black spots represent the pores.

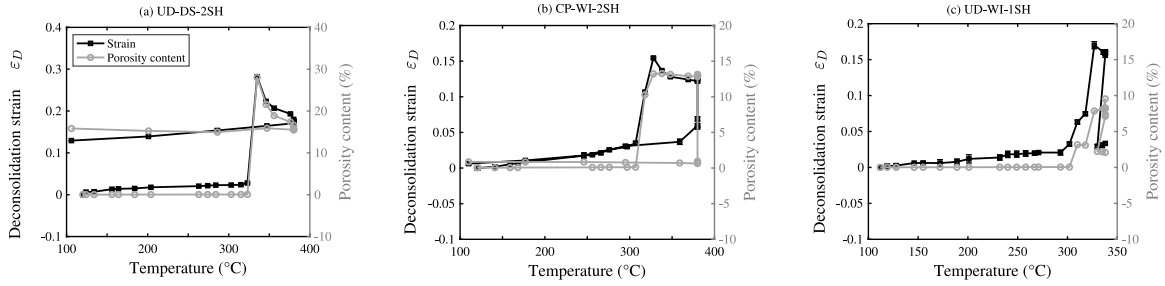

Fig. 9. Deconsolidation strain ε_D and the porosity ϕ of the samples *vs.* sample temperature estimated with the thermal model during the deconsolidation tests: test 2 on UD-DS-2SH (a), test 3 on CP-WI-2SH (b) and test 4 on UD-WI-1SH (c). The dashed circles indicate characteristic temperatures used later for microstructural analysis during deconsolidation.

ϕ during this stage for the considered samples as emphasized in the zoom carried out in Fig. 10, which brings up the following comments. Firstly, this figure proves that the initial porosity ϕ in the samples is very low (< 0.06 %). No significant difference is observed between the UD samples, albeit a slightly higher porosity is seen for the WI sample, and the initial CP sample porosity is higher than that of UD samples. Secondly, above T_g, the increase of porosity ϕ in the UD-WI-2SH sample becomes roughly twice that of the UD-DS-2SH sample (note that the same behavior is not observed in the UD-WI-1SH because of its non-isothermal heating). This suggests that the presence of moisture should induce the enhancement of nucleation/growth of pores, so that the assessed apparent thermal expansion coefficients could be due both to intrinsic thermal expansion mechanisms but also to moisture-induced pore nucleation/growth.

- It is also very interesting from Fig. 10 to note that the onset of stage 2, which corresponds to the drastic increase of deconsolidation, occurs about 20°C earlier in the case of wet samples WI: the onset temperature is around 300°C for them whereas it is around 320°C for the dried ones DS. In addition, the deconsolidation in stage 2 is characterized by sharp shifts in the sample strain and porosity (Figs. 9 and 10). The dried UD-DS-2SH sample exhibits a higher maximum deconsolidation strain and porosity (close to 0.3) than the values reported for the water immersed cross-ply CP-WI-2SH (both close to 0.15). This is *a priori* unexpected and could be caused by a difference in the architecture of the considered fibrous reinforcement, or by the acquisition frequency of the tomographic scans (1 min): the maximum strain of the wet CP-WI-2SH sample may be reached between 318°C and 328°C or between 328°C and 338°C (Fig. 9 b). After the peaks of strain and porosity, it is worth noticing that the deconsolidation strain as well as the porosity decrease while heating the samples up to the dwell. This is directly correlated with the qualitative observations stated in the previous subsection: fibers, which bent during the drastic increase of the porosity, progressively unbend and relax internal stresses, thus yielding in pore closing and decrease of deconsolidation strain.
- During cooling (stage 3) without subjecting samples to a confining pressure (Fig. 9 a), the strain ε_D decreases linearly while the porosity ϕ remains almost constant. This means that while we observe thermal and crystallization shrinkage, it has almost no impact on the porosity induced upon sample heating. When a confining pressure is applied at the end of the dwell, however, fast decreases of both ε_D and ϕ are first recorded, leading to a marked sample reconsolidation (Fig. 9 b–c). Pursuing the cooling

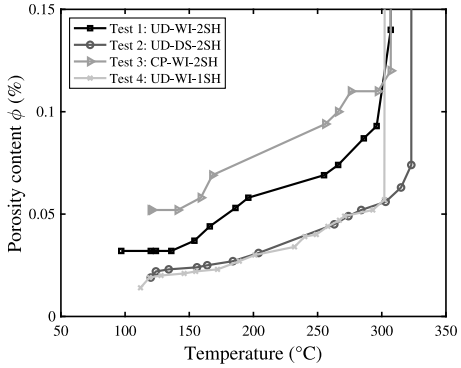

Fig. 10. Zoom of the previous figure showing the porosity ϕ as a function temperature estimated with the thermal model during the deconsolidation tests. The dashed circles indicate the onset temperature of deconsolidation.

still yields to a quasi-linear decrease of ε_D, without noticeable change in ϕ.

3.3. Quantitative analysis at the fiber scale

Pore distribution – The evolution of the spatial distribution of the porosity along the sample thickness ϕ_z is reported in Fig. 11. One clearly sees from graphs (a–c) that ϕ_z are mainly located at the interply interfaces. For the cross-ply (CP) sample (graph b), consecutive peaks are spaced with a distance of ≈0.2 mm, which corresponds to the thickness of a single ply (Fig. 11 b). For the UD samples, the interply interfaces are less obvious but again, most of the peaks are located around the interply region (Fig. 11 a, c). Increasing the temperature during stage 1 leads to a preferential increase of ϕ_z at interply interfaces too; this is especially highlighted in Fig. 11 b. During stage 2, Fig. 11 (d–e) shows that the porosities grow mainly at the vicinities of interply interfaces, since the ϕ_z-peaks are still and mostly located around the interply regions. As revealed by these graphs, this feature seem to be unaffected while changing the sample moisture content. Conversely, the effect of the temperature distribution through the thickness is important and clearly emphasized by comparing graph (d) and (f): one-sided heating localizes the porosity increase only on the bottom of the sample thus affecting the overall deconsolidation dynamics, whereas, two-sided heating allows the deconsolidation to be induced more homogeneously in the samples. Lastly, during stage 3, there is no significant change in spatial distribution during cooling (Fig. 11 h–i).

Pore density – Fig. 12 shows the temperature-evolutions of the pore density $\mathcal{N}_p$ and the porosity ϕ recorded during the deconsolidation experiments. During stage 1, a regular increase of $\mathcal{N}_p$ is observed while at the same time the increase of ϕ is limited. This can be due to the nucleation of novel pores. Moreover, apart from the single point at 120°C with the UD-DS-2SH sample (Fig. 12), the rate of the pore density change $\partial\mathcal{N}_p/\partial T$ for symmetric (and thus more homogeneous) heating conditions seems to increase significantly above the glass transition temperature T_g = 160°C. In this zone, $\partial\mathcal{N}_p/\partial T$ is roughly estimated to 4.1 mm^{-3} K^{-1} for the DS sample and to 11.7 mm^{-3} K^{-1} for the WI one, thus suggesting that moisture should speed up pore nucleation. During stage 2, $\mathcal{N}_p$ together with ϕ first increase drastically. After the deconsolidation peak, there is still a slight increase in pore density $\mathcal{N}_p$ (albeit lower than that observed in stage 1) while the porosity ϕ decreases (Fig. 12 a, c). This can be explained by (i) the nucleation of novel pores (ii) the fact that large pores formed up to the deconsolidation peak probably split into smaller ones (due to the relaxation of internal stresses, see below). During stage 3, it is worth mentioning that $\mathcal{N}_p$ significantly decreases with the application of a confining pressure (Fig. 12 b, c) whereas it is almost constant during cooling whatever the pressure value (Fig. 12 a, b). The last observation suggests again that thermal and crystallization shrinkage has a negligible impact on porosity and pore kinetics. It also suggests that pore nucleation is limited at this stage of the experiments.

Pore size – Fig. 13 (a–c) shows the distribution of the major pore lengths a during stage 1. The majority of pores are initially smaller than 100 μm (small-sized pores) with peak distributions between 10 and 20 μm. By zooming on higher pore lengths, one can notice the appearance of medium-sized pores the length of which lies between 100 μm and 1000 μm after the glass transition temperature T_g (160°C), thus proving pore growth during this stage. However, as emphasized in Fig. 14(a–c), the volume fraction of medium-sized pores is much lower in this stage than that measured for small-sized pores. Combined with results gained for $\mathcal{N}_p$ (previous paragraph), this observation reinforces the scenario of (small) pore nucleation during stage 1 above T_g. During stage 2, Fig. 13 d-f shows that the density of small-sized pores increases drastically up to the consolidation peak, thus showing that pore nucleation should still be important during this sequence. Albeit less pronounced, the increase in density of medium-sized pores, but also large-sized pores (≥ 1000 μm), is also noticeable, proving that, at the same time, important pore growth occurs in the samples. In addition, after the deconsolidation peak, the density of small and medium-sized pores slightly increases. Meanwhile, the volume fraction of large-sized pores decreases whereas that of small and medium-sized pores increases: this is in-line with the qualitative and quantitative observations respectively made in the two previous subsections, *i.e.*, the closing of bigger pores, the decrease of the deconsolidation strain and sample porosity. The closing of larger pores would also be a cause of the slight increase of smaller pores. Lastly, during stage 3, applying a confining pressure leads to a reduction in the density of pores, in particular the bigger ones. In addition, whatever the applied confining pressure, the type of fibrous architecture and heating type, it is interesting to notice that upon cooling, the density of small, medium and large-sized pores practically remained constant. This suggests that either pore nucleation and pore growth/splitting/closure should be limited upon cooling.

Pore morphology – Fig. 15 shows the distribution of pore shapes (defined in Section 2.6) during stages 1 and 2. This figure shows that, initially, the majority of pore shapes are mainly rode-like (prolate) and blade-like (ellipsoidal), mainly oriented along the fiber axis. Pores also exhibit disk-like shapes and rare sphere-like shapes (especially in the case of unidirectional samples). Increasing the temperature in stage 1 does not lead to a significant change in shape distributions, as shown in Fig. 15 (a–c). The same remark is valid during stage 2 (Fig. 15 d–f), except the increase of about 5 % in the proportion of disk and sphere-like shapes.

4. Discussion

Thanks to the unique 3D real-time and *in situ* images provided by synchrotron X-ray microtomography, the microstructures and the deconsolidation mechanisms occurring during the heating and cooling of high performance TPCs could be finely characterized. We could thus emphasize three main processes illustrated in the scheme of Fig. 16 and discussed hereafter.

4.1. Pore nucleation

The first process is pore nucleation. This mechanism is clearly detected from the glass transition temperature T_g at least up to the deconsolidation peak. Within this temperature range, pore nucleation is characterized by the noticeable increase in the density of pores $\mathcal{N}_p$ which, according to the graph shown in Fig. 13, is mainly related to the number of small-sized pores. The induced small-sized pores exhibit mainly rod, blade and disk-like shapes; they are mainly located around

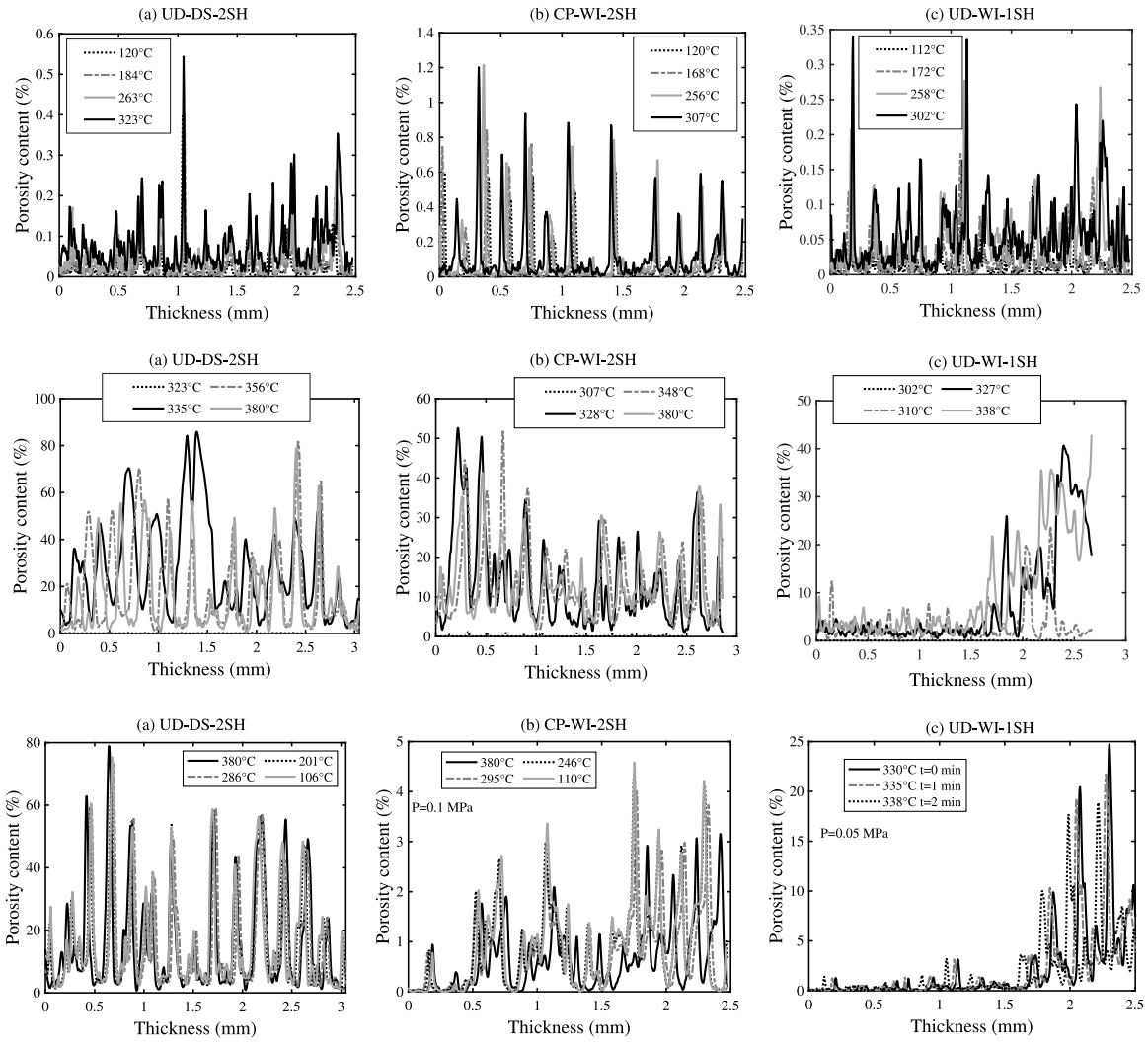

Fig. 11. Evolution of the spatial distribution through the sample thickness porosity ϕ_z during stage 1 (a–c), stage 2 (d–f) and stage 3 (g–i) of the deconsolidation experiments UD-DS-2SH (a,d,g), CP-WI-2SH (b,e,h) and UD-WI-1SH (c,f,i).

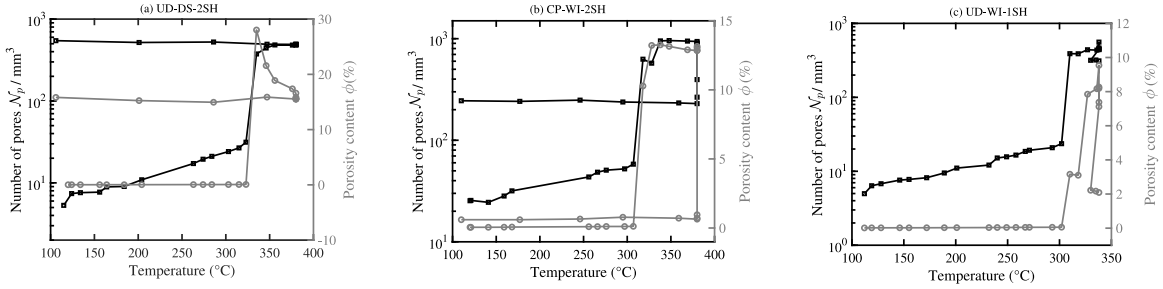

Fig. 12. Evolutions in pore density $\mathcal{N}_p$ and porosity ϕ with the temperature during deconsolidation experiments: UD-DS-2SH (a), CP-WI-2SH (b) and UD-WI-1SH (c).

the laminates' interplies (Fig. 11). Our results also clearly reveal that this process is enhanced/driven by the water content inside the samples tested: the higher the water content, the higher the pore nucleation rate $\partial\mathcal{N}_p/\partial T$. Thus, pore nucleation above T_g may be attributed to several coupled effects related to moisture content and temperature (since the tested prepregs were already subjected to heating above melting during the initial consolidation of the laminates, it is assumed that there are no other residual volatile substances from additives used in TPC prepreg manufacturing). Above T_g, the mechanical properties of the polymer matrix and the matrix-fiber interfaces may be soft enough to allow pore nucleation, this softening being enhanced by the water content which acts as a solvent. In addition, an increase of the free volumes in the polymer matrix may allow porosity nucleation through fine scale moisture evaporation and coalescence. Moisture may also agglomerate and form porosity nucleation sites in polymer-rich areas. This could be backed up by our observations: the high porosity content at the laminates' interply interfaces (Fig. 11) which are the most polymer-rich locations. This process may be enhanced by temperature which promotes moisture transport in the composites [31].

Our results also proved that an initial drying of the sample at 180°C for 72 h does not prevent pore nucleation. We previously assumed that moisture may be stored in the composite in two forms namely

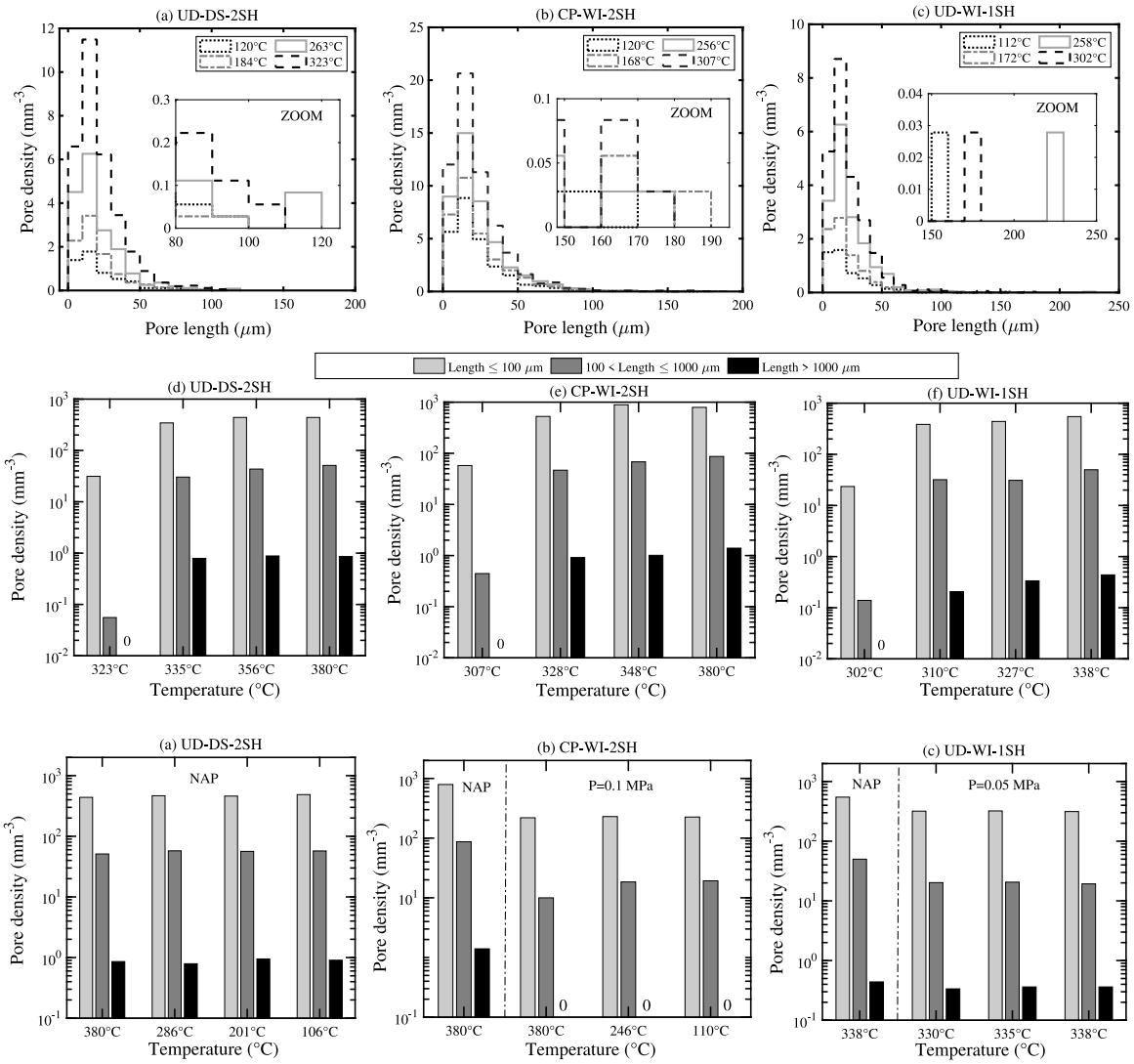

Fig. 13. Distribution of the major pore length a during stage 1 (a–c), stage 2 (d–f) and stage 3 (g–i): UD-DS-2SH (a,d,g), CP-WI-2SH (b,e,h) and UD-WI-1SH (c,f,i) samples.

"weakly bonded water" and "strongly bonded water" [31]. Drying at 180°C for 72 h should effectively remove the "weakly bonded" water but "strongly bonded" water should remain in the composite due to the high thermal energy required to desorb it. The residual moisture strongly bonded to the composite may thus be involved in the nucleation process observed in the dried samples.

Lastly, at the beginning of stage 2, the mechanical properties of the polymer matrix and the fiber–matrix interfaces are soft enough to allow a rapid and sharp increase in deconsolidation. Deconsolidation is then characterized by a sharp increase of the deconsolidation strain. It is driven by the compaction stress stored in the fiberbed during the previous consolidation process. During Hot Press consolidation under 4 MPa, stresses due to fiber bed compaction, shrinkage mechanisms, and eventually skin-core thermal gradient may not fully relax before material solidification. Internal stresses are produced at three different scales [38,39] (fiber, ply and laminate scale), resulting in a complex three-dimensional stress state within the composite laminate [40]. This transverse residual compaction stress acts as a driving force for deconsolidation. With the matrix softening, it enhances the nucleation of small-sized pores [14,41,42]. Finally, above that point of the deconsolidation process, fibers keep on relaxing with unbending. We suspect then that nucleation is limited, the increase in the density of small-sized pores being related to pore splitting/closing (see below) and freezed upon cooling.

4.2. Pore growth

The second important deconsolidation mechanism is pore growth. As emphasized with our results, pore growth is limited during stage 1, does not take place during stage 3, and mainly occurs during the early parts of stage 2, *i.e.*, above the deconsolidation temperature T_D. Indeed, above this temperature, medium- and large-sized pores are induced in the samples, leading to a significant increase in both the sample deconsolidation strain and porosity. The onset pore growth temperature T_D mainly occurs around the melting onset (between 300°C and 310°C) in the case of water immersed (WI) samples and in the melting zone (≥ 310°C) in the case of dried samples (DS). The lower T_D value recorded for wet samples may be attributed to their higher porosity content (Fig. 10) which can weaken the laminates' interfaces, and to moisture-induced softening of the sample's viscoelastic properties [43]. The substantial pore growth observed in the early parts of stage 2 are also attributed to the internal stresses induced during the consolidation process. The transverse elastic energy of the compacted fiberbed is stored at low temperature in the bent fiber and at the fiber/fiber contacts. When the temperature is increasing, the matrix softens down to a critical point where it can no longer withstand the internal elastic energy. At this point, internal stresses are suspected to drive pore growth and decohesion of the interfaces. This agrees with results presented in previous work in [44]. As revealed by the 3D images,

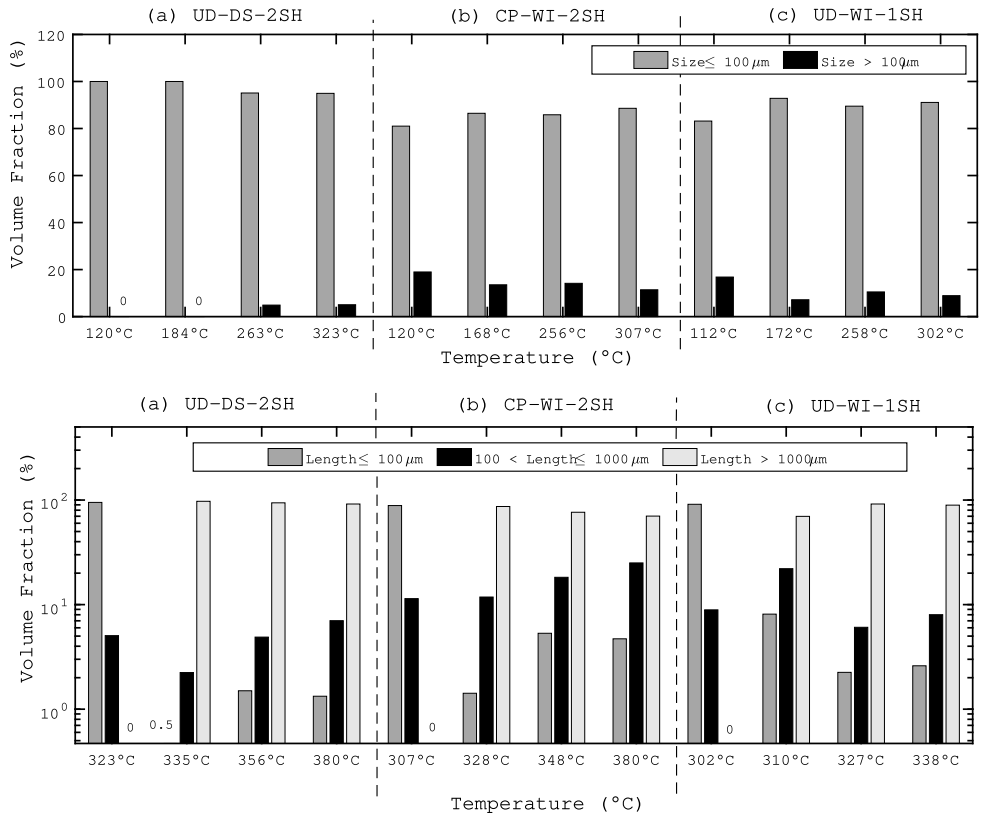

Fig. 14. Volume fraction of small, medium and large-sized pores during stage 1 (a–c) and stage 2 (d–f): UD-DS-2SH (a,d), CP-WI-2SH (b,e) and UD-WI-1SH (c,f) samples.

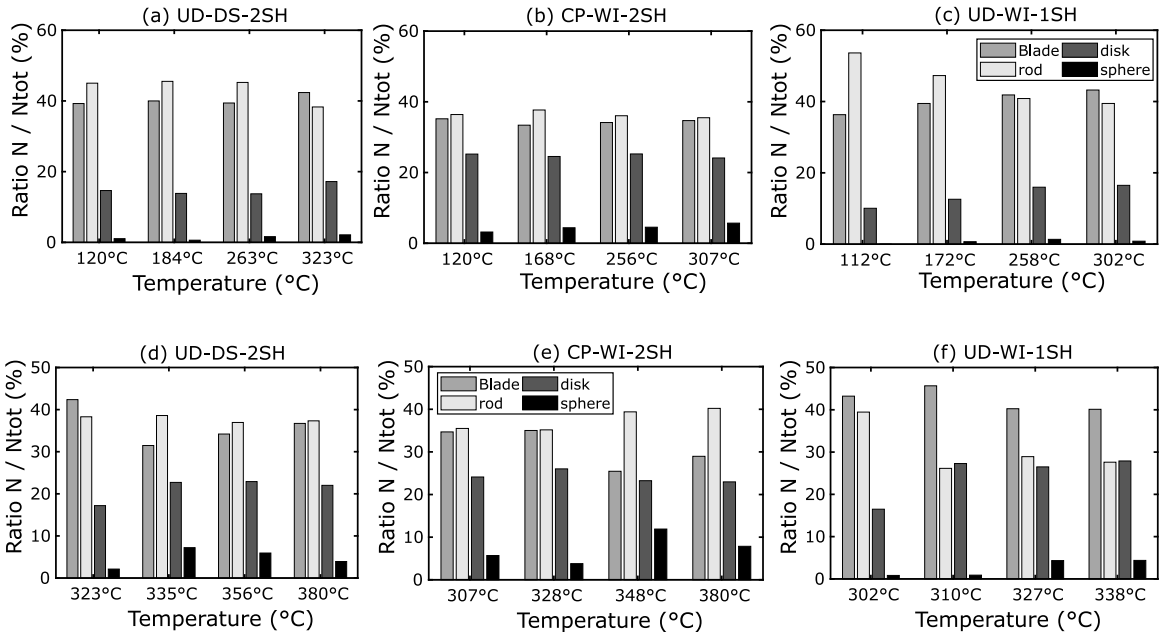

Fig. 15. Distribution of pore shape during stage 1 (a–c) and stage 2 (d–f): UD-DS-2SH (a,d), CP-WI-2SH (b,e) and UD-WI-1SH (c,f) samples.

pores grow by crack propagation and/or coalescence. Additional 3D real-time images at finer scale would be required to (un)validate these hypotheses.

4.3. Pore closure or splitting

The third deconsolidation mechanisms which occur during the end of stage 2 and the beginning of stage 3 are pore closure and/or splitting: during these sequences, our results reveal that pores collapse and/or split into smaller ones, leading to a decrease in the sample strain and porosity. During stage 2, here again, internal stresses are suspected to be the main cause of these pore scale mechanisms. Indeed, after a first strain mode which conducts to fiber bending (see last point), the polymer matrix creep allows bent fibers to recover their initial and unconstrained straight shapes, as emphasized from the 3D images (see Fig. 6 d, e in Section 3.1). Combined with possible gravity forces and

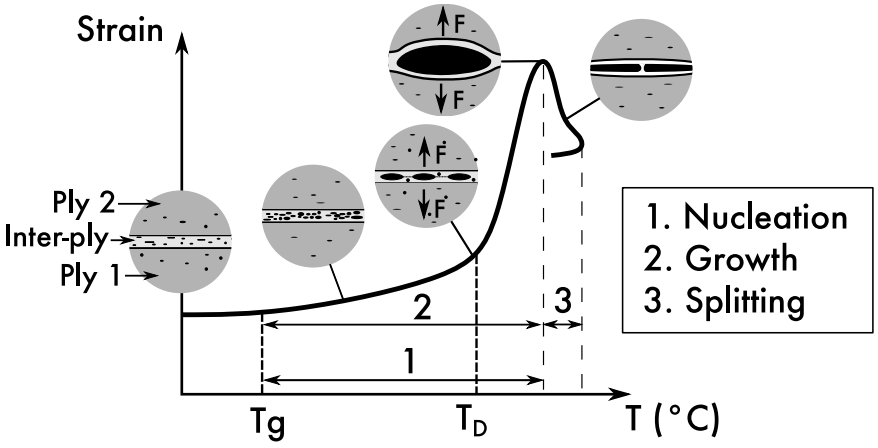

Fig. 16. Schematic representation of deconsolidation process in unidirectional prepreg-based TPC laminates.

capillary effects, this mechanism would induce the observed decreases of the deconsolidation strain, porosity and pore size. In addition, as also revealed by our experimental results, subjecting the samples to an additional confining pressure, as in the beginning of stage 3, drastically enhances these pore closure/splitting mechanisms. For example a low pressure of 0.1 MPa was sufficient to close/split all the large-sized pores but there are still small-sized and medium-sized residual pores (Fig. 13 h, Fig. 9 b). This stage practically determines the final pore content, distribution, size and shape in the composite samples, as thermal or crystallization shrinkages involved during cooling do not lead to a significant change in these descriptors.

5. Conclusion

In this work, dedicated to an experimental investigation of the deconsolidation phenomenon in thermoplastic composites, we were able to deeply investigate the microscopic mechanisms at the origin of the drastic thickness increase observed at the macroscopic scale in several forming or assembly processes. While interrupted tests can be performed by rapid cooling in order to freeze the deconsolidation process, they imply testing several different samples, frozen at different temperatures, so that microstructure evolution cannot be followed directly. By taking advantage of the facilities offered by synchrotron X-ray sources and by designing a dedicated thermomechanical setup, 3D real-time observations of deconsolidation mechanisms in CF/PEKK laminates were successfully carried out. These original observations enable precise tracking of pore nucleation and growth all along representative thermomechanical cycles. Results gained through the analysis of four samples with different stacking or humidity conditioning showed several important features of CF/PEKK deconsolidation:

- Samples tested exhibit a very low initial porosity made of small pores which are mainly located at the vicinity of the inter-plies. These pores are presumably induced during laminate processing.
- Sample deconsolidation is mainly initiated after T_g with early porosity formation that increases regularly until reaching the critical deconsolidation stage. During this stage, the number and size of pores increase with temperature, thus suggesting a mixture of pore nucleation and growth processes. Such evolutions mainly occur at laminate interfaces, *i.e.*, in polymer-rich zones and where the initial porosity was mainly located. During this early stage, increasing the **initial moisture content**, which is suspected to soften the polymer rheology and to add novel nucleation sites, yields to speed up the aforementioned mechanisms.
- At temperatures close to melting temperature, a drastic deconsolidation with a sharp and pronounced increase in deconsolidation strain was systematically observed in our cases. This is associated with an increase in the nucleation of novel pores which rapidly grow and/or coalesce towards large anisotropic pores. These marked slender shapes are partly constrained by the confining anisotropic fibrous reinforcement and question the relevance of the unconfined isotropic bubble nucleation/growth models in literature. This could be explained by the release of internal stresses in the fibrous network enabled by the heat softening of the polymer matrix. Here again, it must be pointed out that the higher the initial moisture content, the softer the polymer rheology, the higher the nucleation sites and thus the earlier the onset temperature of this stage.
- Holding the temperature (dwelling stage) leads to pursuing the internal stress release in the fibers, which progressively unbend towards their initial stress-free straight configurations. Combined with possible gravity effects as well as capillary forces, this yields to a pore closure mechanism, which can be markedly enhanced by subjecting the samples to a confining pressure, however small.
- From a phenomenological and qualitative standpoint, similar deconsolidation mechanisms were observed for the two fibrous reinforcements studied. This should be further analyzed quantitatively with other fibrous architectures. In addition, results obtained in this study emphasize the significant effect of heating conditions, with marked structural gradients with asymmetric heating. This point should also be studied further.

Beyond the contributions summarized above, the present work provides a large statistical database for the development of physically motivated models of deconsolidation. Nevertheless, even though the present approach gives a deep view and understanding of the micromechanisms associated with deconsolidation, it still cannot explain the origin of the driving force of this phenomenon, for which further investigations are needed.

CRediT authorship contribution statement

Luc Amedewovo: Methodology, Validation, Formal analysis, Investigation, Writing, Visualization. **Laurent Orgéas:** Conceptualization, Methodology, Writing – review & editing, Supervision. **Basile de Parscau du Plessix:** Methodology, Writing – review & editing, Supervision, Funding acquisition. **Arthur Levy:** Conceptualization, Methodology, Writing – review & editing, Supervision. **Steven Le Corre:** Conceptualization, Methodology, Writing – review & editing, Supervision, Project administration, Funding acquisition.

Declaration of competing interest

The authors declare the following financial interests/personal relationships which may be considered as potential competing interests: Luc Amedewovo, Steven Le Corre reports financial support was provided by Jules Verne Institute of Technology.

Data availability

Data will be made available on request.

Acknowledgments

The authors would like to acknowledge the funding of PERFORM project led by IRT Jules Verne (French Institute for Advanced Research and Technology) who made this work possible. The authors wish to associate the industrial partners of PERFORM project: Airbus, Safran, Daher, Latecoere, Stelia Aerospace, Clayens NP, Naval Group and Faurecia. The authors would like to thank Arnaud Arrive for the bench setup manufacturing and assembly help. The authors would also like to thank Guillaume Bravais and Sofiane Terzi from Novitom company, who assisted us during the preparation and realization of the experiments at ESRF (Grenoble, France). The 3D reconstruction of the 2D tomographic images was performed by the Novitom company, which is specialized in 3D material characterization, NDT and micro-analysis based on advanced imaging techniques including synchrotron technology. Luc Amedewovo wishes to thank Florent Autrusseau and Clara Aimar for the image processing help.

Appendix A. Temperature estimation in the sample

Temperature in the sample was estimated using numerical modeling.

A.0.1. Thermal model

We used the 1D transient heat Eq. (A.1) following the procedure described in Amedewovo et al. [16].

$$\rho C_p \frac{\partial T}{\partial t} = \frac{\partial}{\partial z}\left(k_z \frac{\partial T}{\partial z}\right) \quad \forall z \in [0, l] \tag{A.1}$$

where ρ is the composite density, C_p its heat capacity, k_z its thickness or transverse conductivity and l its thickness. The physical properties of the CF/PEKK used are also available in Amedewovo et al. [16]. The 1D model was used given the plate-like geometry of the samples and also because the samples were confined during heating, thus limiting convection losses around the samples. Though the 1D model is not suited to account for the forced convection occurring during the cooling stage, it was used and implemented as a slab (representing the composite sample) subjected to two heat flux at its boundaries.

Mixed boundary conditions were considered at both surfaces of the composite plate:

- At the contact with the lower hot platen, the heat flux writes:

$$k_z \frac{\partial T}{\partial z}(z = 0, t) = -\frac{TCL - T}{R_1} \tag{A.2}$$

  where R_1 accounts for the thermal contact resistance between the sample and the lower hot platen, and TCL is the lower hot platen temperature which is considered uniform and known as measured by a monitoring thermocouple (Fig. 2).

- At the upper surface, the heat flux writes:

$$k_z \frac{\partial T}{\partial z}(z = l, t) = \frac{TCU - T}{R_2} \tag{A.3}$$

  where R_2 is the thermal contact resistance between the upper hot platen and the sample upper face. TCU is the upper hot platen temperature also measured by a monitoring thermocouple (Fig. 2). R_2 accounts for both the conducto-convective exchange with the air and the radiative exchange with the facing upper hot platen.

For a given set of constant R_1 and R_2 thermal resistances, the above set of equations was solved with the FE code COMSOL Multiphysics [45]. Spatial integration used quadratic finite elements and time was integrated implicitly with the backward Euler method [16].

A.0.2. Identification of boundary conditions

A standard inverse method was used to identify the thermal resistances R_1 and R_2 used in Eqs. (A.2) and (A.3). The residual consists of the differences between the modeled and measured temperature for each of the three embedded thermocouples (Fig. 2) at each time step over the temperature cycles. The residual 2-norm was minimized using the simplex method built in MATLAB [46].

The obtained values of thermal resistances are given in Table A.2.

For each heating configuration, the thermal resistances before (No Applied Pressure) and after pressure application are provided.

A.0.3. Thermal model validation

The temperature residuals at the sample middle (TC2), lower (TC1) and upper face (TC3) are plotted versus time in Fig. A.17. The range of the error is ±5°C for one-sided heating (Fig. A.17 a) and ±3°C for two-sided heating (Fig. A.17 b). The high peaks observed during the dwells are related to the moment when the pressure was applied. The second high peak observed at the cooling beginning is due to the forced convection which is not taken into account in the 1D model (Fig. A.17 b). Moreover, the inverse method identification was performed using temperature measurements up to 380°C. At this temperature, sample deconsolidation may occur, resulting in changes to the composite thermal properties. A thorough estimation of the sample temperature field would require a more in-depth study taking into account the appearance of porosity during heating.

The developed thermal model thus allowed us to estimate the composite laminate temperature during the deconsolidation experiments. In the case of two-sided heating, the sample temperature was estimated as the average of the simulated temperature field over the sample thickness. In the case of one-sided heating, deconsolidation can be expected to start at the sample's lower face. The sample's lower face temperature is thus estimated as the average of the simulated temperature field over a thickness corresponding to the three first bottom plies.

Appendix B. Supplementary material

Supporting data are available at doi:10.17632/g7r7fkhtz7.1.

Table A.2
Thermal resistances in (m^2 K W^{-1}) identified by inverse method for different pressures.

	One-sided heating (1SH)		Two-sided heating (2SH)	
	NAP	P = 0.05 MPa	NAP	P = 0.1 MPa
R_1	0.50×10^{-2}	0.67×10^{-5}	0.21×10^{-1}	0.68×10^{-2}
R_2	0.33×10^{-1}	0.68×10^{-5}	0.11×10^{-1}	0.59×10^{-2}

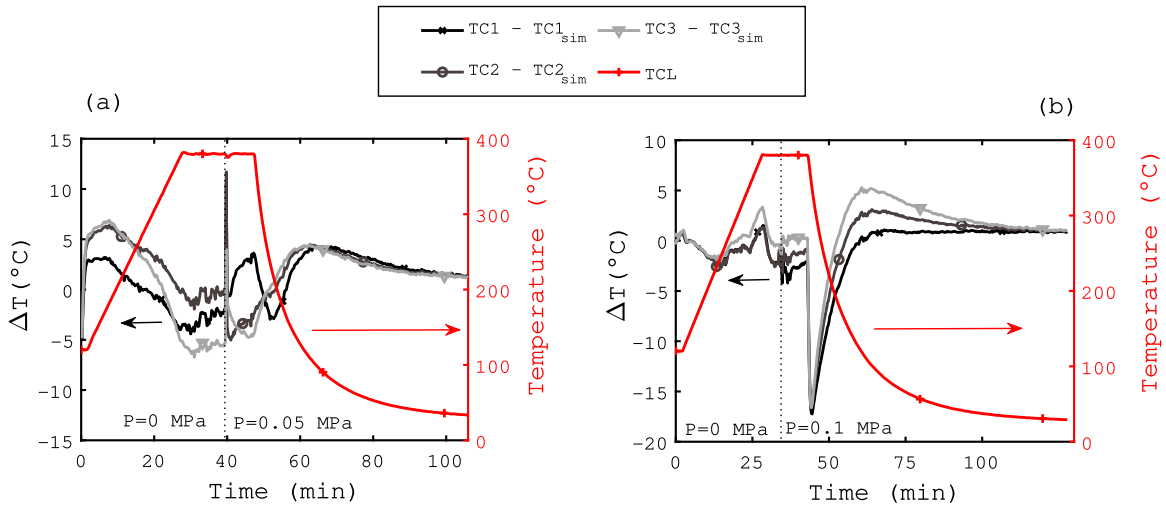

Fig. A.17. Thermal model validation for the two heatings at different pressures: one-sided heating with NAP + $P = 0.05$ MPa (a) and two-sided heating with NAP + $P = 0.1$ MPa (b).

References

[1] Hagstrand PO, Bonjour F, Månson JAE. The influence of void content on the structural flexural performance of unidirectional glass fibre reinforced polypropylene composites. Composites A 2005;36:705–14.

[2] Shi H, Villegas I Fernandez, Bersee HEN. Strength and failure modes in resistance welded thermoplastic composite joints: Effect of fibre-matrix adhesion and fibre orientation. Composites A 2013;55:1–10.

[3] Liu X, Chen F. A review of void formation and its effects on the mechanical performance of carbon fiber reinforced plastic. Eng Trans 2016;64:33–51.

[4] Grunenfelder LK, Nutt SR. Void formation in composite prepregs–effect of dissolved moisture. Compos Sci Technol 2010;70(16):2304–9.

[5] Anderson J, Altan M. Formation of voids in composite laminates: coupled effect of moisture content and processing pressure. Polym Compos 2014.

[6] de Parscau du Plessix B. Analyse et modélisation du développement de porosités lors de la cuisson de pièces composites thermodurcissables hautes performances (Ph.D. thesis), Université de Nantes; 2016.

[7] Leterrier Y, G'sell C. Formation and elimination of voids during the processing of thermoplastic matrix composites. Polym Compos 1994;15:101–5.

[8] Roychowdhury S, Gillespie JW, Advani SG. Volatile-induced void formation in amorphous thermoplastic polymeric materials: I. Modeling and parametric studies. J Compos Mater 2001;35:340–66.

[9] Shi H, Fernandez Villegas I, Bersee HEN. Analysis of void formation in thermoplastic composites during resistance welding. J Thermoplast Compos Mater 2017;30:1654–74.

[10] Slange TK, Warnet LL, Grouve WJB, Akkerman R. Deconsolidation of c/PEEK blanks: on the role of prepreg, blank manufacturing method and conditioning. Composites A 2018;113:189–99.

[11] Lu M, Ye L, Mai YW. Thermal de-consolidation of thermoplastic matrix composites-II. "migration" of voids and "re-consolidation". Compos Sci Technol 2004;64:191–202.

[12] Ye L, Chen ZR, Lu M, Hou M. De-consolidation and re-consolidation in CF/PPS thermoplastic matrix composites. Composites A 2005;36:915–22.

[13] Wolfrath J, Michaud V, Månson JAE. Deconsolidation in glass mat thermoplastic composites: Analysis of the mechanisms. Composites A 2005;36:1608–16.

[14] Ye L, Lu M, Mai Y-W. Thermal de-consolidation of thermoplastic matrix composites-I. Growth of voids. Compos Sci Technol 2002;62:2121–30.

[15] Donadei V, Lionetto F, Wielandt M, Offringa A, Maffezzoli A. Effects of blank quality on press-formed PEKK/Carbon composite parts. Materials 2018;11.

[16] Amedewovo L, Levy A, de Parscau du Plessix B, Aubril J, Arrive A, Orgéas L, Le Corre S. A methodology for online characterization of the deconsolidation of fiber-reinforced thermoplastic composite laminates. Composites A 2022;107412.

[17] Picher Martel GP, Levy A, Hubert P. Squeeze flow of randomly-oriented strands thermoplastic composites. In: Proceedings of the 19th international conference on composite materials, Montreal, Canada. 2013, p. 1864–72.

[18] Galvez-Hernandez P, Jimenez-Martin C, Smith R, Mavrogordato M, Maes V, McMahon T, et al. In-situ CT of out-of-autoclave composites manufacturing processes. In: International conference on manufacturing of advanced composites. 2022.

[19] Sentis DF, Orgéas L, Dumont PJJ, Du Roscoat SR, Sager M, Latil P. 3D in situ observations of the compressibility and pore transport in sheet moulding compounds during the early stages of compression moulding. Composites A 2017;92:51–61.

[20] Laurencin T, Dumont PJJ, Orgéas L, Le Corre S, Martoïa F, du Roscoat SR, et al. 3D real time and in situ observation of the fibre orientation during the plane strain flow of concentrated fibre suspensions. J Non-Newton Fluid Mech 2022;104978.

[21] Latil P, Orgéas L, Geindreau C, Dumont PJJ, Du Roscoat SR. Towards the 3D in situ characterisation of deformation micro-mechanisms within a compressed bundle of fibres. Compos Sci Technol 2011;71(4):480–8.

[22] Vilà J, Sket F, Wilde F, Requena G, González C, LLorca J. An in situ investigation of microscopic infusion and void transport during vacuum-assisted infiltration by means of X-ray computed tomography. Compos Sci Technol 2015;119:12–9.

[23] de Parscau du Plessix B, Lefébure P, Boyard N, Corre SL, Lefèvre N, Jacquemin F, et al. In situ real-time 3D observation of porosity growth during composite part curing by ultra-fast synchrotron X-ray microtomography. J Compos Mater 2019;53(28–30):4105–16.

[24] Hernández S, Sket F, Molina-Aldareguı JM, González C, LLorca J, et al. Effect of curing cycle on void distribution and interlaminar shear strength in polymer-matrix composites. Compos Sci Technol 2011;71(10):1331–41.

[25] Centea T, Hubert P. Measuring the impregnation of an out-of-autoclave prepreg by micro-CT. Compos Sci Technol 2011;71(5):593–9.

[26] Larson NM, Cuellar C, Zok FW. X-ray computed tomography of microstructure evolution during matrix impregnation and curing in unidirectional fiber beds. Composites A 2019;117:243–59.

[27] Torres JJ, Simmons M, Sket F, González C. An analysis of void formation mechanisms in out-of-autoclave prepregs by means of X-ray computed tomography. Composites A 2019;117:230–42.

[28] Perez-Martin H, Mackenzie P, Baidak A, Brádaigh CM, Ray D. Crystallinity studies of PEKK and carbon fibre/PEKK composites: A review. Composites B 2021;223:109127.

[29] Avenet J. Assemblage par fusion de composites à matrice thermoplastique: Caractérisation expérimentale et modélisation de la cinétique d'auto-adhésion hors équilibre (Ph.D. thesis), Université de Nantes (UN); 2021.

[30] Pérez-Martín H, Mackenzie P, Baidak A, Brádaigh CM, Ray D. Crystallisation behaviour and morphological studies of PEKK and carbon fibre/PEKK composites. Composites A 2022;106992.

[31] Amedewovo L, Levy A, de Parscau du Plessix B, Orgéas L, Le Corre S. Online characterization of moisture transport in a high-performance carbon fiber-reinforced thermoplastic composite at high temperatures: Identification of diffusion kinetics. Composites B 2023;256:110629.

[32] Paganin D, Mayo SC, Gureyev TE, Miller PR, Wilkins SW. Simultaneous phase and amplitude extraction from a single defocused image of a homogeneous object. J. Microscopy 2002;206(1):33–40.

[33] Schindelin J, Arganda-Carreras I, Frise E, Kaynig V, Longair M, Pietzsch T, et al. Fiji: An open-source platform for biological-image analysis. Nature Methods 2012;9(7):676–82.

[34] Yaniv Z, Lowekamp BC, Johnson HJ, Beare R. Simpleitk image-analysis notebooks: A collaborative environment for education and reproducible research. J Digit Imaging 2018;31(3):290–303.

[35] Arganda-Carreras I, Kaynig V, Rueden C, Eliceiri KW, Schindelin J, Cardona A, et al. Trainable weka segmentation: A machine learning tool for microscopy pixel classification. Bioinformatics 2017;33:2424–6.

[36] Zingg T. Beitrag zur schotteranalyse (Ph.D. thesis), ETH Zurich; 1935.

[37] Angelidakis V, Nadimi S, Utili S. Elongation, flatness and compactness indices to characterise particle form. Powder Technol 2022;396:689–95.

[38] Favre J-P. Residual thermal stresses in fibre reinforced composite materials- A review. J Mech Behav Mater 1988;1(1):37–53.

[39] Parlevliet PP, Bersee HEN, Beukers A. Residual stresses in thermoplastic composites—A study of the literature—Part I: Formation of residual stresses. Composites A 2006;37(11):1847–57.
[40] Shokrieh MM. Residual stresses in composite materials. Woodhead publishing; 2014.
[41] Gent AN. Cavitation in rubber: A cautionary tale. Rubber Chem Technol 1990;63(3):49–53.
[42] Horgan CO, Polignone DA. Cavitation in nonlinearly elastic solids: A review. Appl Mech Rev 1995;48(8):471–85.
[43] Coulson M, Quiroga Cortés L, Dantras E, Lonjon A, Lacabanne C. Dynamic rheological behavior of poly (ether ketone ketone) from solid state to melt state. J Appl Polym Sci 2018;135(27):46456.
[44] Amedewovo L, Levy Arthur, de Parscau du Plessix B, Orgéas L, Le Corre S. Characterization of driving mechanisms involved in deconsolidation of thermoplastic composite laminates. In: ICCM23. Belfast, UK; 2023.
[45] COMSOL Multiphysics® v.6.0., URL https://www.comsol.com, COMSOL AB, Stockholm, Sweden.
[46] MATLAB (R2022a). The MathWorks Inc., Natick, Massachusetts.